 doi:10.20944/preprints202207.0138.v1

Article

Local Morphology and Internal Architecture of the Kawajiricho 2018 Debris-flow Deposit (Hiroshima, Japan)

Christopher Gomez [1,2,*], Kenta Imai [1], Anggri M. Setiawan [2], Danang Sri Hadmoko [2], Junun Sartohadi [3],Aditya Saputra [4],and Balazs Bradak [1]

[1] Kobe University, Faculty of Oceanology, Laboratory of Sediment Hazards and Disaster Risks (Japan); christophergomez@bear.kobe-u.ac.jp
[2] Universitas Gadja Madah, Faculty of Geography (Yogyakarta, Indonesia);
[3] Universitas Gadja Madah, Faculty of Agriculture (Yogyakarta, Indonesia);
[4] Universitas Muhammadiyah Surakarta, Faculty of Geography (Surakarta, Indonesia);

* Correspondence: christophergomez@bear.kobe-u.ac.jp

Abstract: Debris-flows are recurrent events on mountain- and hill- slopes, and they have been the object of numerous field investigations and sampling, however most of this work reposes on imagery and outcrop analysis, in such a way that there are still only a handful of studies investigating the internal architecture of these events' deposits. In the present contribution, we aims at underneath the internal structure of a portion of a debris-flow deposit that was accessible in the aftermath of the 2018 heavy-rainfall debris-flows in Hiroshima Japan. Using a Ramac Pro-Ex GPR with 500 MHz and 800 MHz antenna, a set of longitudinal and transversal transects was used to characterize the deposit. The results demonstrated that a set of subhorizontal layers have filled the valley, and interacting with local terrace edges, these layers have piled up and overcome the obstacle. Across the valleys, a set of trough suggest the presence of channels that were also filled during the event. Finally, in the channel post-event, a set of radargram "cross-bedded units" shows that the final deposition in the channel was of a more dilute flow, typical of a Newtonian flow. This set of units was not to be found at the surface of the post-event pseudo-surface, suggesting that the flow ended as a debris-flow on this surface, and that it is only when the flow dug the final channel that the nature of the flow returned from debris-flow to Newtonian flow.

Keywords: Debris-flow; Hazard; Ground Penetrating Radar; Mountain hazards;

1. Introduction

According to the official reports of the Ministry of Land, Infrastructure, Transport and Tourism (MLIT) of Japan, the heavy rainfall event of July 2018 struck the majority of West Japan. During the span of 11 days from June 28th to July 8th , it generated rainfalls that accumulated to 1214.5 mm in Gifu prefecture, 617 mm in Hyogo prefecture, 1852 mm in Kouchi prefecture, 859 mm in Fukuoka prefecture, 904.5 mm in Saga Prefecture and 697.5 mm in Nagasaki prefecture [1]. In the Kure area of Hiroshima prefecture, the values also exceeded 500 mm in the span of a few days (Fig. 1).

This event triggered an estimated 1,748 sediment-related hazards, of which 567 where debris flows, 55 landslides and 1126 rock collapses, turning into a total of 119 casualties [1]. Such events are predicted by the scientists of the IPCC to only worsen with climate change impacts in the future [2]. To better estimate associated hazards and risks at the local scale in the aftermath of the 2018 heavy rainfall event in Hiroshima, numerical simulations have provided reliable spatial distribution of debris-flow spans [3], while satellite remote sensing and LiDAR data models provided estimates of sediment transfers [4]. The mobilized volumes of debris (V) related to the area (A) following a general trend of $V = 0.285A^{1.127}$ [4].

Preprints (www.preprints.org) | NOT PEER-REVIEWED | Posted: 8 July 2022 doi:10.20944/preprints202207.0138.v1

Both numerical simulations and remote-sensing methods however are not providing any information on the internal structure of the debris-flow deposits and the erosion that may also exist underneath deposits [5]. Moreover, the internal structure of a deposit, and the presence of clasts and other debris trapped within a deposit is essential knowledge for understanding the debris-flow processes and also forecast forthcoming debris-flow hazards and impacts on infrastructures. Indeed, from the surface, blocks are largely visible if there is not a large portion of fine material that recovers it at the end of the debris-flow, or if water-flow erodes the finer fractions. Otherwise, the surface does not depict a true picture of the deposit. Debris-flows being made of heterometric material, often unconsolidated [6] makes traditional methods ineffective to retrieve the internal architecture of the deposits. This is why scientists have turned to geophysics and Ground Penetrating Radar (GPR) to image the otherwise invisible subsurface even when the material is loose on steep talus [7]. Furthermore, the method has also allowed the demystification of the representativity of outcrops in sedimentology and geomorphology, showing that what one can see from the outcrop of a debris-flow deposit may not be representative of the deposit's structure at all [8].

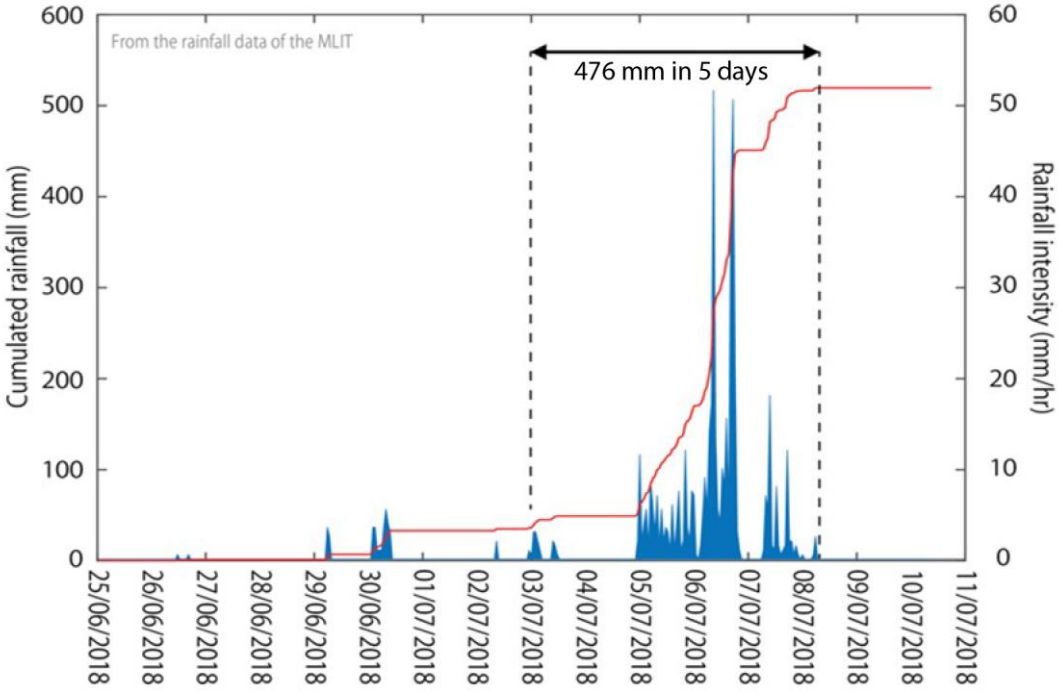

Fig. 1 Cumulated rainfalls (red curve) and rainfall intensity per hour (blue plot), for the period of the 25th June 2018 to 11 July 2018 showing the high intensity and volume rainfall that occurred in the Kure area over a period of slightly less than a week.

Consequently, the present contribution aims to define the internal architecture of the debris-flow deposit and to define whether large blocks are trapped in the deposit, that is widely recovered by finer-fraction material, as well as the potential internal structure, which may have escaped to aerial visual observations.

2. Materials and Methods

The present research occurred in the Kawajiricho valley, using Ground Penetrating Radar, for which topographic data were generated using UAV photogrammetry.

2.1 Research Location

The present research location is in the vicinity of the Nigata Bay, East of Kure-City in the Hiroshima prefecture. It is a coastal area of pocket beaches separated by coastal reliefs, which are cut into graniodiorites, granites with intercalated welded tuff, made of

Preprints (www.preprints.org) | NOT PEER-REVIEWED | Posted: 8 July 2022 doi:10.20944/preprints202207.0138.v1

dacites (Fig. 2.1). At the survey location, the lower part of the valley is cut in coarse-grained graniodiorites, whereas the upstream section of the valley cuts through granite dikes and fine-grained graniodiorites (Fig. 2-1). The surveyed valley was fully impacted by the debris-flow of 2018 and both terraces and the river floor were recovered by the deposits, while other sections were eroded (Fig. 2-2).

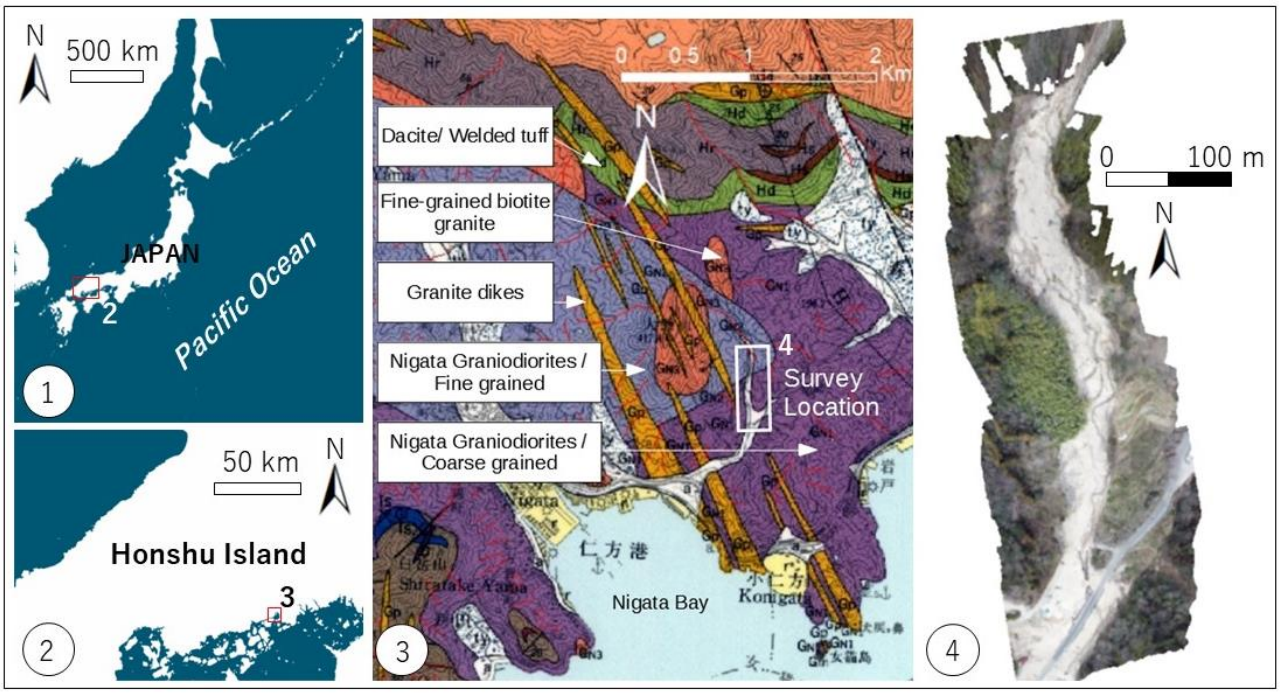

Fig. 2 Location and Geological map of the survey area. The survey location is located in West Japan (1), on the coast of Honshu Island (2) near Hiroshima, just above the bay of Nigata (3). The survey itself occurred in a stream less than 1 km long (4). The UAV data of the field location extends on the fine-grained Nigata graniodiorites, but the GPR and sediment density assessment only occurred in the coarse-grained Nigata graniodiorites. The talweg is understood to be a mixture of the different Nigata graniodiorites, material from the dikes and the fine-grained biotite granite, which have created the surface formation in white on map 1. The Geological map was adapted from the geological map available online as a WMS file for GIS, produced by the Japanese Geological Survey (www.gsj.go.jp).

Although the heavy-rainfall events of 2018 brought the subsurface material to light (Fig. 2.2), the slopes where the debris-flow started are mostly covered in forests, which are dominated by the tree plantations of *Sugi* and *Hinoki*. Historically, however, Japanese mountains have been either deforested for timber harvest and firewood. The aerial photograph of 1948, just after World War 2 is showing that the investigated catchment was mostly deforested, and that only the upper slopes were forested (Fig. 3). These deforested areas have already been prone to erosion in the past as it can be seen from the 1961 aerial photograph, were locally high-reflectance values shows bare ground. In 2009, however, the catchment was already fully reforested, including the valley floor. In 2018, the debris-flow, although catastrophic only reactivated the valley floor area and the forested slopes remained unaffected.

Preprints (www.preprints.org) | NOT PEER-REVIEWED | Posted: 8 July 2022 doi:10.20944/preprints202207.0138.v1

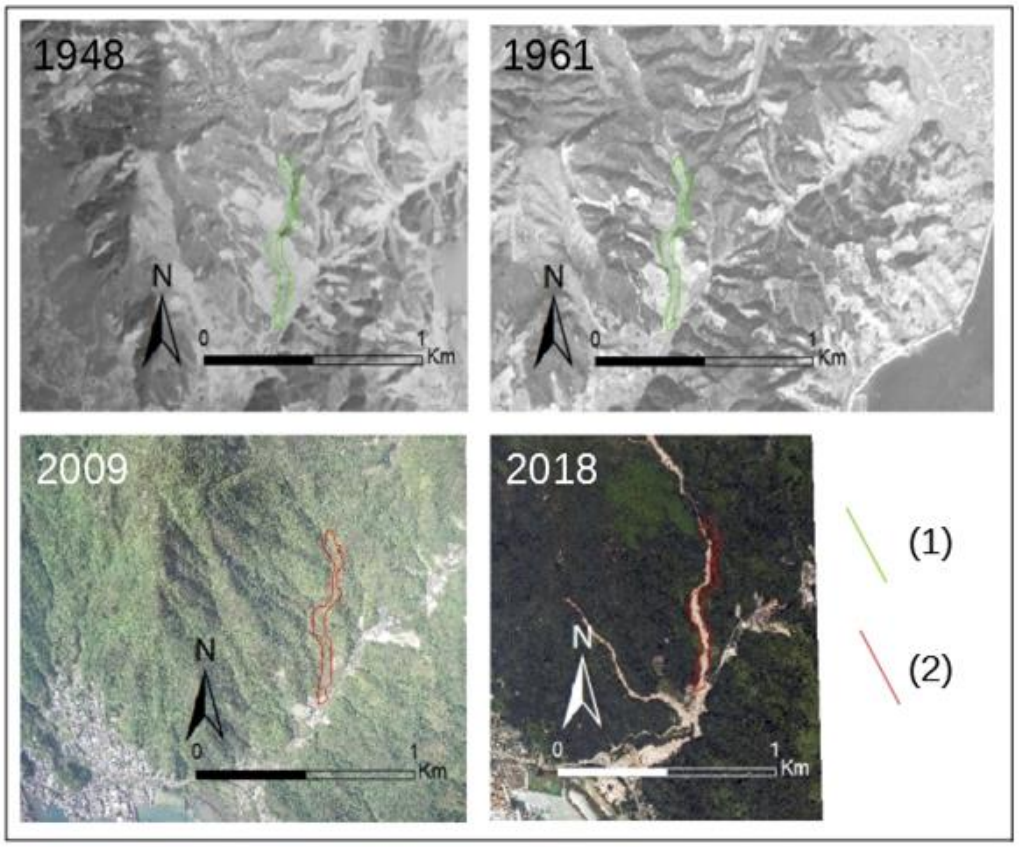

Fig. 3 Evolution of the land cover between 1948 and 2018, using the aerial photograph series of 1948, 1961, 2009 and 2018. (1) is the limit of the paddy fields at the valley floor where the debris flow occurred and (2) is the same limit, but after conversion into field abandonment and replacement with forestry plantation (imagery from the Geospatial Authority of Japan, www.gsi.go.jp).

2.2 Topographic Data acquisition and construction

Although the present study is not a topographic study per se, a topographic dataset was generated in order to position the Ground Penetrating Radar data and to eventually correct for topographic variations would have it become necessary.

The UAV data was collected in the field using a Phantom 4-Pro and a Mavic-Pro, both manufactured by DJI®. Using the standard onboard camera, the geotagged imagery was recorded and exported into the Structure-from-Motion and Multiple-View-Stereophotogrammetry software Metashape Pro, commercialized by Agisoft®. The photographs were first loaded in the software and 8 tie-points were added on the photographs to help the calculation. The tie-points as well as the Ground Control Points (GCPs) used for the calculation were measured using a Sunway total-station to coerce the model in 3D. The oriented model from the UAV-imagery was merged with the data from the total station using 3 identifiable points. These points were used to convert the local frame of reference from the total station into real-world coordinates. The local RMSE in Z was calculated to be < 20 cm, between the point-cloud and a set of 10 GCPs obtained from the total station. The accuracy of the georeferenced dataset remained the same as the one from the UAV GNSS data (meter-scale horizontal accuracy). As this low-accuracy positioning is only used to place the study on a map, only the relative position is relevant for the present study.

Once the model was tied to the field-data, the sparse point cloud was generated, and then densified using the Multiple-View Stereophotogrammetric procedure, with aggressive point filtering on and no limit to the number of points created. The point-cloud was then meshed to create a dataset (2.5D instead of 3D), which was then converted into

Preprints (www.preprints.org) | NOT PEER-REVIEWED | Posted: 8 July 2022 doi:10.20944/preprints202207.0138.v1

a traditional DEM (Digital Elevation Model). Areas with vegetation were ignored. Finally, an orthophotographs of the debris-flow deposit was generated, so that the location of the Ground Penetrating Radar transects could be confirmed.

2.3 Ground Penetrating Radar

Ground Penetrating Radar (GPR) is a geophysical method that uses the propagation properties of electromagnetic waves in the ground. These properties were first revealed when a plane from the US Air-force flying above Greenland thought its radar was giving it clearance to the ground to a 1000 m, when in fact the aircraft was already dangerously to the surface of the ice. After the crash, the analysis of the flight recorders revealed that the radar was seeing through the ice, and not the surface of the ice. This was the start of the development of numerous ground penetrating radar to investigate the ice structure, mainly using the velocity profiles of the GPR data. Rapidly this method extended to soil investigation, at first in areas where limited processing was providing convincing results, such as on sand dunes () and river sands and gravels (), before being extended to more challenging environments, such as complex volcanic deposits (), pyroclastic flow deposits (), and derived lahars (), where volcanic minerals can have an important effect on the data. Silicate-rich volcanoes with pumiceous material (Izu-Ooshima, Karthala…) can be relatively challenging to image using GPR for instance.

The GPR used in the present investigation is a Mala® RAMAC Pro-Ex mounted with 500 MHz and 800 MHz antennas and connected optic-fiber cables to optimize data transfer and reduce cabling noise. The system was then connected by Ethernet cable to a Panasonic Toughpad from which the system was controlled using the GroundVision 2.0 GUI interface. The data was collected using the coding-wheel, to have a regular spacing between each trace along the profile. This is essential to reconstruct the geometry of the subsurface, and also to perform the hyperbola-slope analysis to determine the velocity of the electromagnetic signal in the subsurface.

The signal processing was performed following the same pattern for each single GPR transect, so that they could be compared: (1) "dewow" was applied to the signal in order to erase the signal energy travelling straight from the emitting to the receiving antenna; (2) the first signal amplitude change was moved to 0, in order to eliminate the time travelled through the air between the bottom of the antenna and the ground. Even if the travel distanced is very short, as the signal travels to "close-to" light speed, it represents a relatively important span of time. (3) Then the gain of the data was modified using AGC gain (automatic Gain Control), with a window opening on the full signal time (98 ns) and with a factor of 1.17, with the maximum gain set not to saturate the signal amplitude. (4) Then horizontal features and repeats that can be noise in the system, was deducted from the signal using a 100 traces moving-window average. This also removed part of the ringing effect between the air and the surface, which masked the top part of the signal. (5) Then, the topography was added to the signal, and as the topographic changes are only of a few 10s of centimeters with no sharp slope change, no migration for the topography was applied. (6) The signal was then migrated from two-way time signal to a depth signal using a velocity model that was crated from the slopes of hyperbolas. The hyperbolas defined velocities at 0.06 and 0.07 m.ns-1 for the majority of the signal, except near the ground surface in relative "low" topographies, where the velocity changed to 0.13 m.ns-1. The signals were then exported for visual analysis as image files (those provided in the figures), and the signal were also exported after step 2 in Matlab for numerical analysis of the relative dielectric permittivity ($\varepsilon_r = \frac{\varepsilon_0}{\varepsilon}$ [Unitless = F.m / F.m]).

Preprints (www.preprints.org) | NOT PEER-REVIEWED | Posted: 8 July 2022 doi:10.20944/preprints202207.0138.v1

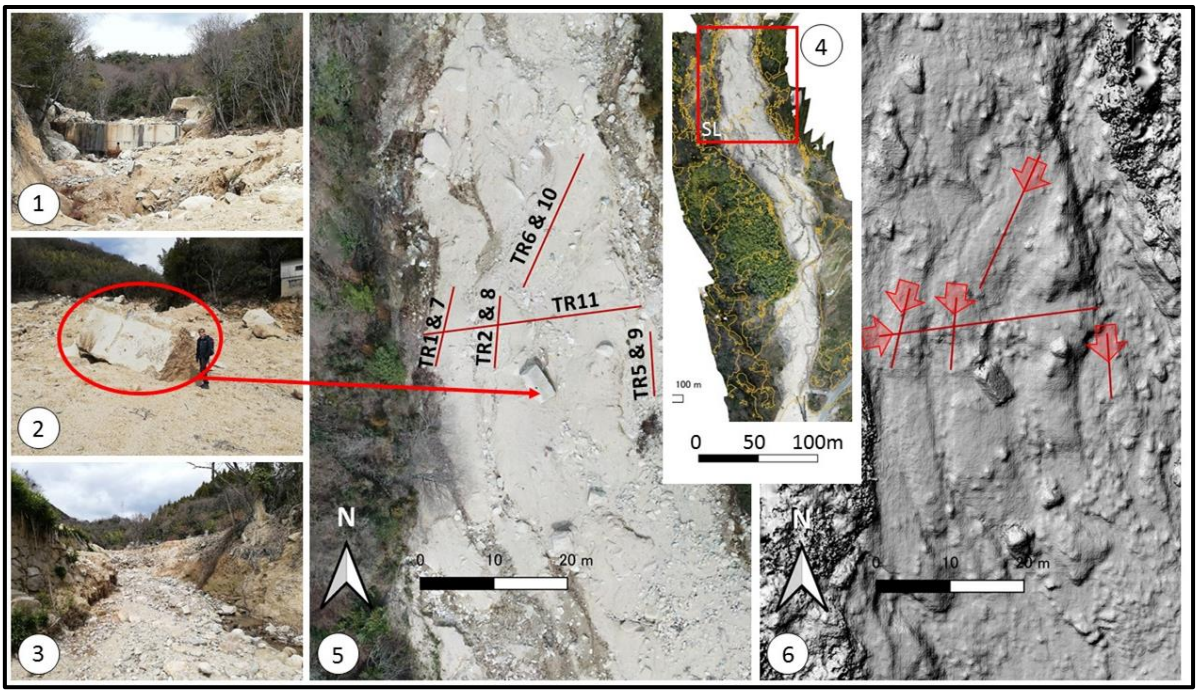

Fig. 4 Location of the Ground Penetrating Radar transects and their orientation in the field. (1) upstream-ward photograph showing the check dam impacted by the debris flow event; (2) Block of the check dam transported by the debris flow with correspondence on the central aerial photograph; (3) photograph near the road showing the previously cultivated terraces on the side and the debris flow deposit in the center; (4) orthophotograph derived from UAV photogrammetry showing the study area where the GPR investigation occurred; (5) Location of the 9 GPR transects, with transects 1,2,5 and 6 obtained from the 800 MHz shielded antenna and transects 7 to 11 obtained from the 500 MHz shielded antenna.

3. Results

The results of this research are composed of 9 GPR radargrams (radargrams 1, 2, 5 and 7 to 11; n.b. that the radargram numbering correspond to data acquisition numbers and are kept to ease data sharing). Transects 7 to 9 (Fig. 5) provide a longitudinal window on the internal structure of the deposit down to 3.5 m depth with the 500 MHz antenna, while the 800 MHz antenna (Tr.1,2,5) offers a zoom on the first two meters (Fig. 5). Transects 1 and 7 show that a set of semi-horizontal units with apparent backset organization characterizes the subsurface. This means that the lower unit tends to have a further downstream extension compared to the unit above. A sharp limit from these units and the layers underneath exists at 2 m between 0 and 10 m distance, and then this unit rises sharply to < 1 m around 12 m, creating a step. The layers above and underneath the step are all interlaced with numerous blocks that appear as hyperbolae, some of which suggest the presence of very large blocks. Both in the 500 MHz and 800 MHz radargrams appear hyperbolae showing the GPR signal entering the block, then leaving the block (Fig. 5-a) between 0.5 and 2 m distance and around 1 m depth. At the location of transects 8 and 2, similar sub-horizontal units were also detected, although more irregular in detail, as the limits between the units are less linear and show undulations (Fig. 5 Tr. 2). The lower part of the radargram also shows numerous blocks-generated hyperbolae, like it did at transects 7 and 1. However, the limit between this "lower layer" and the top units is much closer to the ground, with a depth ~1m. The last "short transect" in the direction of the talweg is located ~ 2 m to 2. 5 m lower topographically and it is characterized by a different internal organization. The organization of the units could be characterized as "cross-bedded" (to use a sedimentology analogy, but one needs to keep in mind that it is, in the present case, the radargram interpretation). This time, however, there is no clear contact between the top layers and the lower part of the radargram. It is rather a transition compared to the clear limits that could be seen in the two other sets of radargrams.

Preprints (www.preprints.org) | NOT PEER-REVIEWED | Posted: 8 July 2022 doi:10.20944/preprints202207.0138.v1

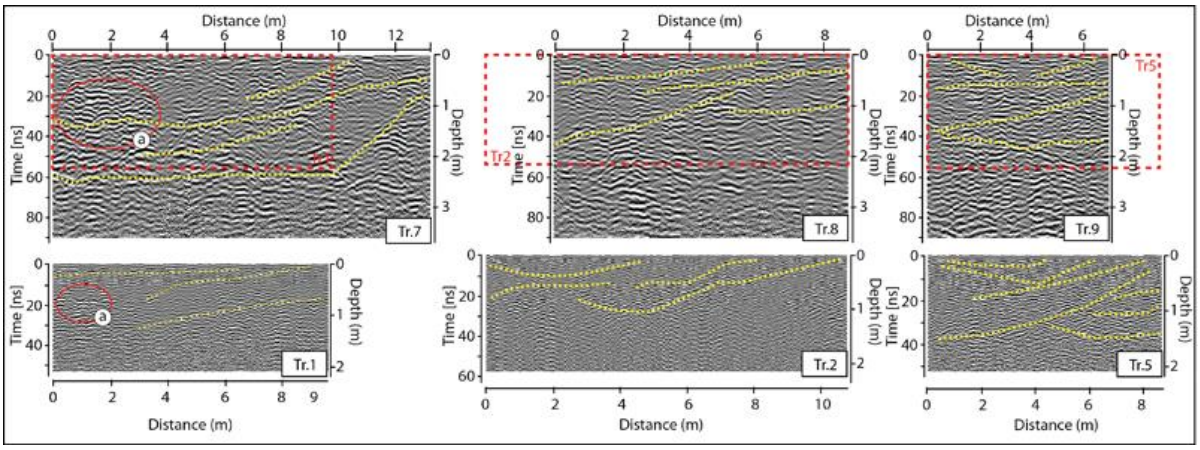

Fig. 5 The six < 13 m transects with the 500 MHz and the 800 MHz antennas (See Fig. 4 for location). Each transects shows series of lenticular units, which can be attributed to either local scouring. Using the signal characteristics, the bedrock is at 2 m depth for transects 7 and 8, while on transect 9, at 1.8 m depth, the signal differs significantly.

Completing these first three radargrams taken parallel to one another, two longitudinal transects taken slightly upstream (Fig. 4) show a set of subhorizontal layers (Fig. 6). The two radargrams located on top of one another also display layers that are shorter in reach, appearing as elongated lenses, and like for the first three radargrams, all the layers are reach in blocks (Fig.6 a,b and c). Both blocks a and c where confirmed by digging the subsurface during the GPR field acquisition.

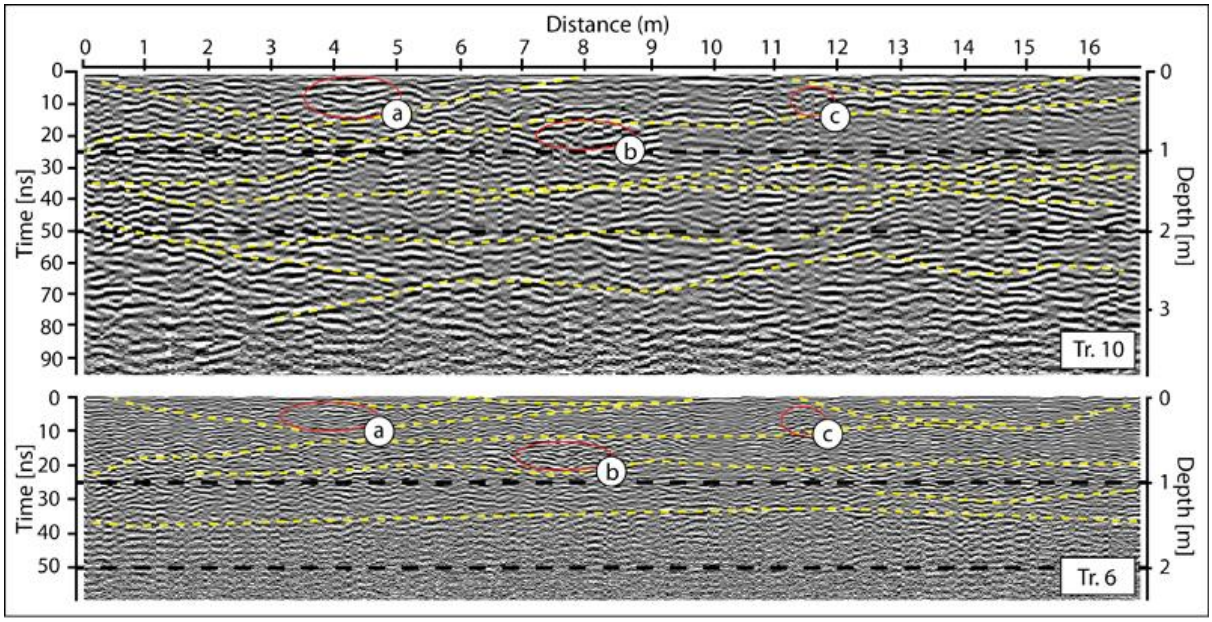

Fig. 6 Transects 10 and 6 collected using the GPR antenna 500 MHz and 800 MHz. The horizontal black dashed-lines at 1 and 2 m depth are used to relate the two radargrams to one another.

The transects transversal to the valley direction displays a set of units, that is more complex than the longitudinal extension (for this reason, we also represented the layers without the radargrams in Fig. 7). In the first 10 to 20 cm, the surface is characterized by horizontal units, or units with slight dipping angles (Fig. 7-1 & 2). The units limits also show undulations, but compared to the longitudinal layers, the limits are steeper, creating series of “filled depressions”.

Preprints (www.preprints.org) | NOT PEER-REVIEWED | Posted: 8 July 2022 doi:10.20944/preprints202207.0138.v1

The top set of units shows relative dielectric permittivity ranging from 2,000 [unitless] to > 4,000 [unitless] (Fig. 7-3). These two values define two groups of air – immediate subsurface transition, with a topographic division, where the low topographies between 0 and 23 m are characterized by the lower ξ_r, while the high topography has a higher ε_r, showing that in low topography the dielectric permittivity of the material is closer to the vacuum dielectric permittivity. As the relative permittivity is 1 ($\varepsilon_0/\varepsilon_0$) for free space and range up to 80 for freshwater (for instance clay ε_r =4 to 40, and wet sand ε_r= 20 to 30), it can be inferred that the first few 10 cm in the low topographies is either (1) having a lower density with a relative increase of the dry void ratio. On the contrary, the material of high topographies is wetter and or denser.

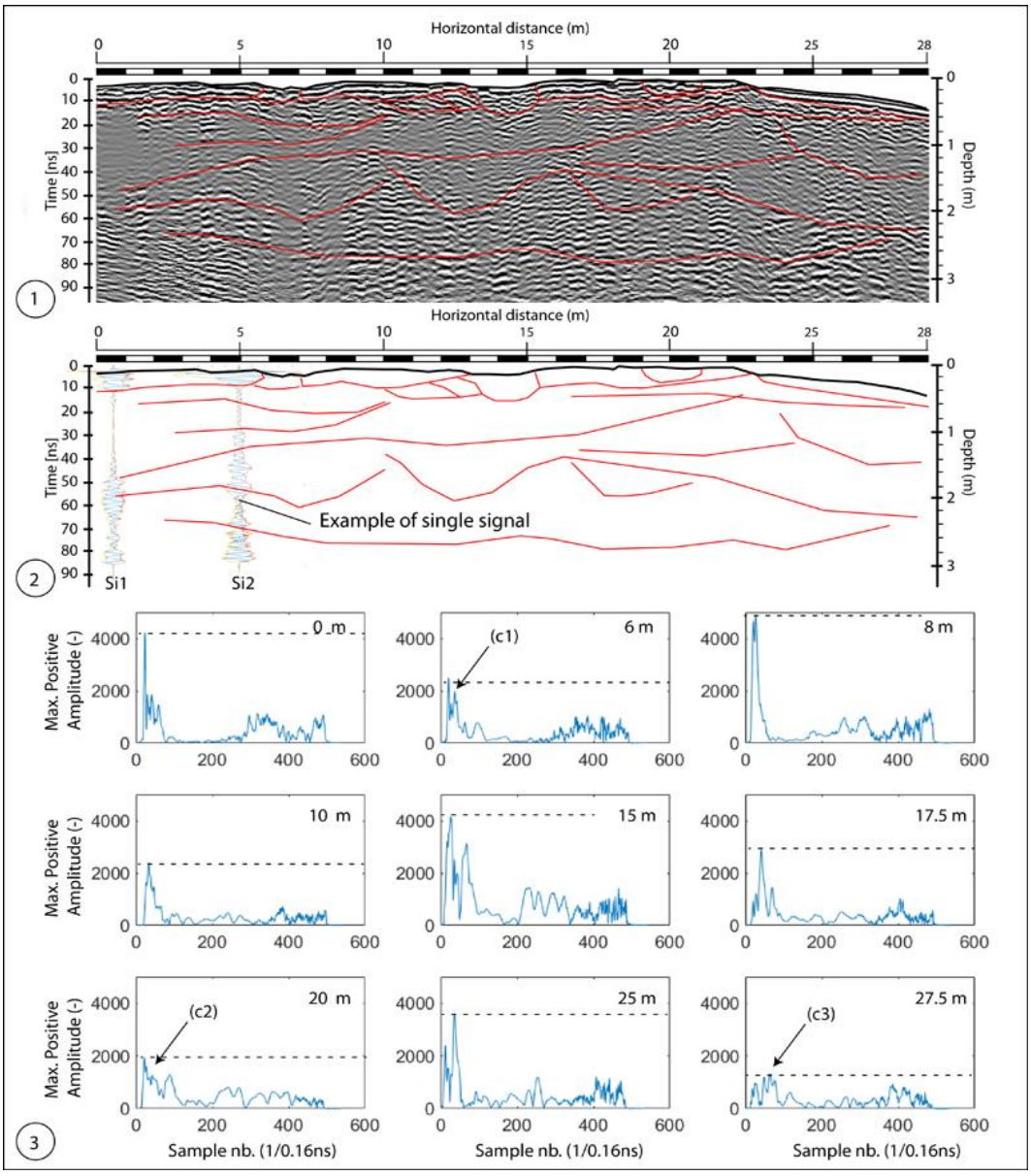

Fig. 7 GPR cross-section (Tr11) of the valley from the true right to the true left, with the main GPR data characteristics. (1) Radar cross-section corrected for topography and velocity; (2) Units defined by change in local signal amplitude, following spatial linear patterns. The layers defined are GPR layers and not strictly sedimentary units (a layer can be created by a change in grain-size, ground-water limit...). Si1 and Si2 are two examples of a single signal at location 50 cm and 5 m, with the signal envelope added. (3) Maximum positive amplitude of single signals at different distances along the transect, with the time represented as a sample number (important to understand the level of time discretization, explaining the relative permittivity amplitude. The maximum amplitude, near the time (0) always display the maximum amplitude as the signal changes from a velocity of

 doi:10.20944/preprints202207.0138.v1

0.3 $m.ns^{-1}$ in free air to a variable 0.07 $m.ns^{-1}$ to 0.13 $m.ns^{-1}$, the faster signal corresponding to the block rich surface, while the fine-dominated surface provides a slower velocity.

4. Discussion

Debris-flow deposits have arguably more to offer than their surface characteristics. In the present contribution, we have seen that sets of units or layers extend subhorizontally in the valley direction, except in the lower-part of the river bed where the water was flowing post-event. The radargram across the valley did however show different units and layers, with undulations that can be interpreted as erosion channels that have been filled. The longitudinal transects are showing a set of subhorizontal units, which seem to have stopped at the contact of a local talus or terrace nose (Fig. 5 Tr7), and piled up against it. Providing that the layers were deposited by the present event, then the depression in Fig. 7 can be explained as potentially the results of local channeled flows, or some other forms of erosive features that have been filled.

However, in comparison with other studies of GPR in debris-flows, such complex forms have never been detected, and one should be cautious with this interpretation. Indeed, in New Zealand, Starheim et al. [9] imaged a debris-flow deposit using Ground Penetrating Radar. The debris-flow was in its simplest form, i.e. only a few meters wide, and about 100 m length and from an open-slope. The layers only showed the results of a plug-flow. The layers were wrapping above one another, but underneath, this plug flow clearly generated an erosion of the substratum it deposited on. If several plug flows occurred next to one another, or consecutively, like it happens for fan formation, then it could explain the three filled-up grooves that are found at this location. Similar GPR radargrams from a debris-flow deposit at the Cotopaxi have also shown similar patterns, which have been interpreted to be trough and fill due to channeled activity [10].

In valley-confined settings, the investigation of debris-flow deposits have been mostly done in volcanic settings. At Semeru Volcano in Indonesia, it was found that debris-flow deposits were typically displaying subhorizontal layers that extend longitudinally, although laterally complex units imbrication exists, like series of lenses [8]. On the valley floor, the contact with buried section of sediment-check dams or locally rising lava-flow deposits also showed similar climbing and retrogradation until the unit level rose above the obstacle level [11].

5. Conclusions

From the GPR investigation and the radargram investigation, one can infer that:

(1) The debris-flow deposited subhorizontal, crude units constituting up to the first two meters of the post-deposition pseudo-terrace;
(2) The deposit in the post-event channel are characteristics of Newtonian river flow with cross-bedded units, and these units could not be found on top of the pseudo-terrace, i.e. the pseudo-terrace was constructed by the debris-flow phase and it is during the more "water-rich" phase that incision occurred.
(3) Locally, however, incision occurred in the flow, as the presence of three troughs attest for. These may be short-lived temporary channels that were generated by erosion.
(4) These findings are consistent with other GPR studies on debris-flow deposits and fan deposits generated by debris-flows.

Author Contributions: All the authors participated in field work and data acquisition. Data assimilation was generated by the authors at Kobe University and the first author wrote the manuscript.

Funding: This research was co-funded by Kobe University, Dept. of Maritime Sciences, the international collaboration fund of the same department as well as the IMARC research funding lead by Dr. Gomez.

Data Availability Statement: All the GPR data are available upon request.

Acknowledgments: The author would like to thank Dr. Britta Sannel of Stockholm University for participating in one of the field trip related to the present research project.

Conflicts of Interest: The authors declare no conflict of interest.

References

References must be numbered in order of appearance in the text (including citations in tables and legends) and listed individually at the end of the manuscript. We recommend preparing the references with a bibliography software package, such as EndNote, ReferenceManager or Zotero to avoid typing mistakes and duplicated references. Include the digital object identifier (DOI) for all references where available.

1 MLIT, 2018. Damage caused by sediment-related disasters due to the heavy rain of July 2018 (in Japanese, accessed online city.kure.lg.jp/uploaded/attachment/35112.pdf).
2 IPCC AR4; Cambridge University Press: Cambridge, UK, 2007.
3 Takebayashi, H.; Fujita, M. Numerical Simulation of a Debris Flow on the Basis of a Two-Dimensional Continuum Body Model. *Geosciences*, **2020**, 10, 45, 1-20.
4 Miura, H. Fusion Analysis of Optical Satellite Images and Digital Elevation Model for Quantifying Volume in Debris Flow Disaster. *Remote Sensing*, **2019**, 11,1096, 1-19.
5 Kataoka, M.; Ashikaga, K.; Miyata, S.; Gomez, C. Laboratory Simulation of debris-flow Inundation Fan Under Varying Sediment Characteristics. **2022.** *71st Sabou-gakkai Meeting in Miyazaki, abstract*, 131.STP-12. (in Japanese).
6 Gomez, C.; Shionhara, Y.; Tsunetaka, H.; Hotta, N.; Bradak, B.; Sakai, Y. Twenty-Five Years of Geomorphological Evolution in the Gokurakudani Gully (Unzen Volcano): Topography, Subsurface Geophysics and Sediment Analsysis. **2021**. *Geosciences*, 11, 457, 1-24.
7 Sass, O.; Krautblatter, M. Debris flow-dominated and rockfall-dominated talus slopes: Genetic models derived from GPR measurements. **2007**, *Geomorphology*, 86, 176-192.
8 Gomez, C.; Lavigne, F. Transverse architecture of lahar terraces, inferred from radargrams: preliminary results from Semeru Volcano, Indonesia. **2010**. *Earth Surf Process Landf*, 35-6, 1116-1121.
9 Starheim, C.A.; Gomez, C.; Harrison, J.; Kain, C.L.; Brewer, N.J.; Owen, K.; Hadmoko, D.S.; Purdie, H.; Zawar-Reza, P.: Owens, I.: Wassmer, P.; Lavigne, F. Complex Internal Architecture of Debris-Flow Deposit Revealed Using Ground-Penetrating Radar, Cass, New Zealand. **2013.** *N. Z. Geogr.* 69, 26-38.
10 Ettinger, S., Manville, V., Kruse, S., Paris, R. GPR-derived architecture of a lahar-generated fan at Cotopaxi volcano, Ecuador. **2014.** *Geomorphology* 213, 224-239.
11 Gomez, C.; Lavigne, F.; Hadmoko, D.S.; Wassmer, P. Insights into lahar deposition processes in the Curah Lengkong (Semeru Volcano, Indonesia) using photogrammetry-based geospatial analysis, near-surface geophysics and CFD modelling. **2018.** *J. Volcanol. Geotherm. Res.* 353, 102-113.